Publication 5

Simas Rackauskas, Kimmo Mustonen, Terhi Järvinen, Marco Mattila, Olga Klimova, Hua Jiang, Oleg Tolochko, Harri Lipsanen, Esko I. Kauppinen, and Albert G. Nasibulin. 2012. Synthesis of ZnO tetrapods for flexible and transparent UV sensors. Nanotechnology, volume 23, number 9, 095502, 7 pages.

Synthesis of ZnO tetrapods for flexible and transparent UV sensors

Simas Rackauskas[1*], Kimmo Mustonen[1], Terhi Järvinen[1], Marco Mattila[2], Olga Klimova[3], Hua Jiang[1], Oleg Tolochko[3], Harri Lipsanen[2], Esko I. Kauppinen[1] and Albert G. Nasibulin[1*]

[1] NanoMaterials Group, Department of Applied Physics, Aalto University, Puumiehenkuja 2, 00076, Espoo, Finland

[2] Department of Micro and Nanosciences, Micronova, Aalto University, Tietotie 3, 02015 Espoo, Finland

[3] Material Science Faculty, Saint-Petersburg State Polytechnical University, Polytechnicheskaya 29, 195251, Saint-Petersburg, Russia

email: simas.rackauskas@tkk.fi, albert.nasibulin@aalto.fi

Abstract. ZnO tetrapods (ZnO-Ts) were synthesized in a vertical flow reactor by gas phase oxidation of Zn vapor in an air atmosphere. Morphology of the product was varied from nearly spherical nanoparticles to ZnO-Ts, together with the partial pressure of Zn and reaction temperature. MgO introducing during synthesis, increased the band gap, optical transparency in a visible range and also changed ZnO-T structure. Fabricated flexible transparent UV sensors showed 45 fold current increase under UV irradiation with the intensity of 30 μW/cm^2 at the wavelength of 365 nm and response time of 0.9 s.

Keywords: Kinetic growth, tetrapods, UV sensor, ZnO.

1. Introduction

Zinc oxide (ZnO) is a direct wide band gap (3.37 eV) semiconductor material with a large exciton binding energy (60 meV). It has gained significant attention because of the unique optical, piezoelectric and magnetic properties, as well as capability of band gap tuning [1, 2]. Non-catalytically grown ZnO nanostructures can be observed in various morphologies such as nanowires [3], nanobelts [4], nanobridges and nanonails [5], nanoshells [6], tetrapods [1, 7-19]. The latter is one of the most gorgeous structures with many promising applications in solar cells [9], lasers [10, 20], field emitters [14], UV and gas sensors [7, 11].

Zinc oxide tetrapods (ZnO-Ts) were discovered in smoke from zinc-smelting plants and first studied in chemical vapor deposition systems [21, 22]. ZnO-Ts were produced in the lab scale through hydrothermal process [11], vapor synthesis from ZnO and C mixture [23], or directly from Zn powder, when tetrapods are collected on reactor walls [13, 16] or filtered at the outlet [17]. Direct synthesis of ZnO-Ts from the metal vapor has obvious advantages of low temperature process and high yield, still the control of uniform concentration is rather difficult.

In this work, we designed and constructed a vertical flow reactor for the controlled synthesis and collection of ZnO-Ts. In order to find favorable synthesis conditions, we varied the growth temperature and Zn vapor pressure. In order to modify the band gap and transparency of ZnO-Ts, we introduced magnesium vapor during the tetrapod growth. Applicability of the produced ZnO-T structures was examined by fabricating transparent and flexible UV sensors.

2. Experimental methods

ZnO-Ts were synthesized by a gas phase oxidation of Zn vapor in an air atmosphere. The synthesis reactor consisted of a vertical quartz tube inserted in a furnace, a metal evaporator inside the tube and the product collection system (Fig. 1). A vertical orientation of the reactor was used to minimize recirculation associated with the buoyancy forces. The metal evaporator was a stainless steel tube filled with Zn powder (99.999% purity) mixed with SiO_2 carrier granules (99.99% purity) with the size of 0.2 - 0.7 mm. 1 g of the mixture, consisting of 2/3 wt. % zinc and 1/3 wt.% SiO_2 was placed on a supporting net in the evaporator. The temperature of the evaporator was measured using a K-type thermocouple, mounted underneath the

supporting net. A position of the evaporator was adjusted to be the same as the furnace temperature. Argon (99.999%), purified from oxygen containing species by an oxygen trap (Agilent OT3-4), was utilized as a carrier gas through the evaporator at the flow rate of 0.3 L/min. An outer air flow was introduced in the reactor at the flow rate of 1.0 L/min. The flow behavior was maintained to be laminar with the Reynolds number varying from 220 to 330 depending on experimental conditions. An average residence time in the reactor was varied from 1.9 to 2.6 s. Produced tetrapods were collected downstream of the reactor on a nitrocellulose filter with a pore size of 0.45 μm. The collection time was varied from 5 to 30 minutes. For introducing MgO a certain amount of Mg powder was added to the Zn-SiO_2 mixture.

The product was investigated by scanning and transmission electron microscopes (SEM JEOL JSM 7500F and TEM JEOL 2200FS with double aberration correctors). Crystalline structure was examined by X-Ray Diffraction technique (Bruker D8 Advance). Absorbance was measured by UV-vis-NIR dual-beam spectrophotometer (Lambda 950, Perkin-Elmer). Photoluminescence (PL) measurements were carried out at room temperature using a HeCd laser operating at 325 nm for excitation at an average intensity of about 20 W/cm^2. The sample PL was spectrally resolved in a monochromator and detected using a photomultiplier tube and lock-in techniques.

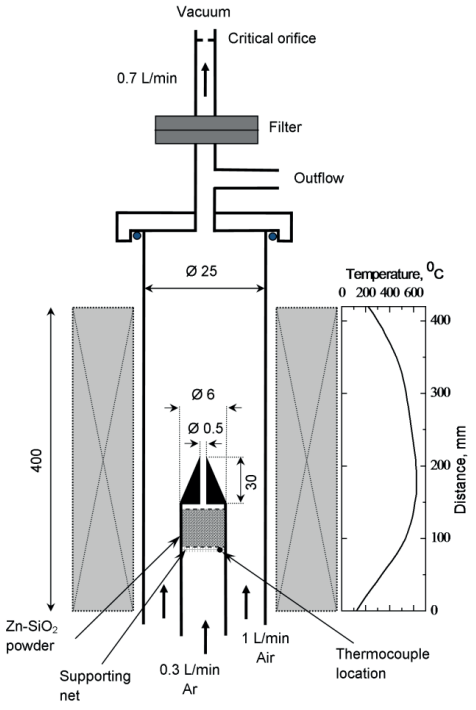

Figure 1. Schematics of the vertical flow reactor. Dimensions are given in mm.

3. Experimental results and discussion

3.1. Synthesis of ZnO-Ts

At the temperature of 500 °C and below, only particles with the diameter of 50-200 nm were produced (Fig. 2a). It can be noticed that some particles have short tetrapod legs (inset in Fig. 2a). At the temperature of 600 °C, an increase in the Zn partial pressure results in the drastic change in the particle morphology: from nearly spherical particles to thick and short leg tetrapod structures (Fig. 2b). From the leg structure one can assume the screw dislocation growth mechanism, as it was shown for ZnO nanowires [24]. Further temperature increasing to 700 °C led to ZnO-Ts with high aspect ratio legs (diameter 10-20 nm and length up to 0.5 μm) as shown in Fig. 2c. From TEM image presented in Fig. 3a it can be seen that each ZnO-T leg is a single crystal. Increasing the temperature to 750 °C caused the formation of polycrystalline plates on ZnO-T legs (Fig. 3b).

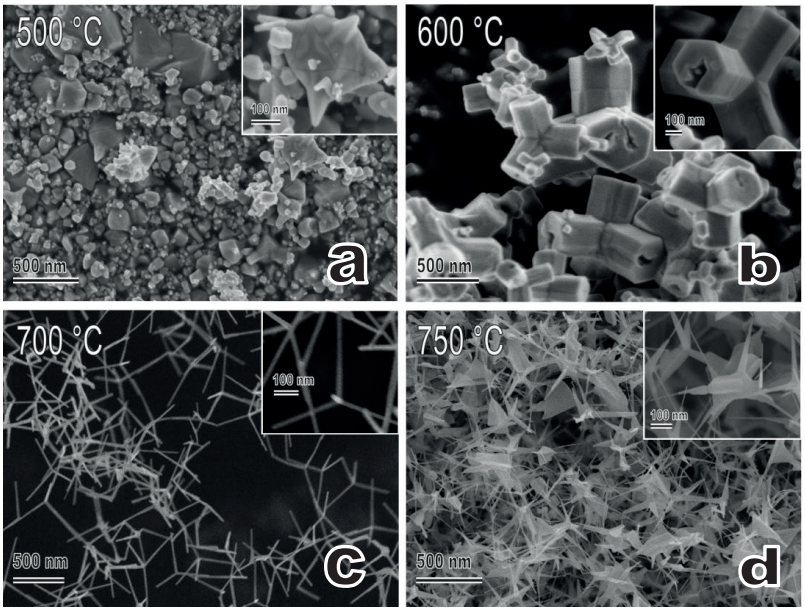

Figure 2. SEM images of ZnO structures synthesized at different temperatures. Insets are close up images.

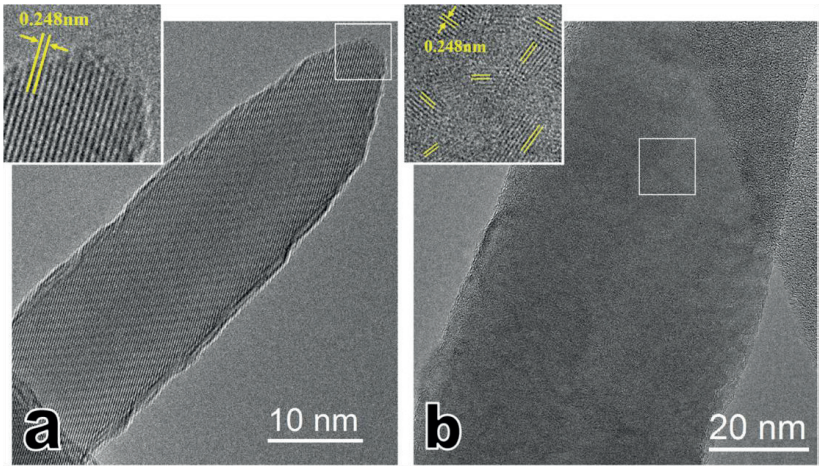

Figure 3. HR-TEM images of ZnO-T legs, synthesized at: a) 700 °C, b) 750 °C. Insets are the close ups, showing lattice fringes.

Growth of tetrapod structures of ZnO [1] and other II-IV semiconductors [21] was explained by the formation of zinc blende nucleus, out of which wurtzite legs grow [8]. Formation of such highly anisotropic shapes as tetrapods requires a kinetic growth regime, when the rate of the monomer arrival is greater than its diffusion on the surface [21, 25]. At low growth rates, under thermodynamic control, spherical nanocrystals are formed. When the growth rate is increased, preferential growth at most reactive sites is expected.

The overall trend of ZnO-T morphology change is summarized in Fig. 4. From our experimental data one can see that at 500 °C there is no considerable kinetic growth, only very few particles have anisotropic growth sites and grew short tetrapod legs. At 600 °C, Zn partial pressure increases and higher growth rate and anisotropic structure are observed (Fig. 2b). However, even at 600 °C, Zn vapor pressure is low, which favors higher nucleus diameter also lower kinetic growth rate and consequently resulted in ZnO-T structures with low aspect ratio. At 700 °C high anisotropy structures were obtained because of high Zn vapor pressure, favoring small nucleus diameter and fast kinetic growth. If the temperature is further increased, large number of small diameter particles are produced, which further aggregate into polycrystalline plates (Fig. 2d and 3b) having nearly ordered structure in one direction. Such spontaneous oriented attachment of primary particles

is explained by oriented aggregation, which is caused by a substantial reduction in the surface free energy [26, 27].

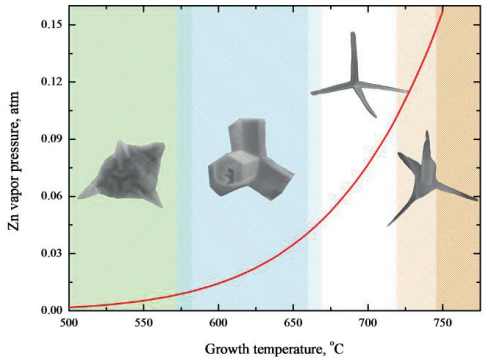

Figure 4. ZnO-T morphology at different temperatures and vapor pressures. Tetrapods shown are not in the scale.

3.2. Vapor phase MgO introduction

In order to introduce MgO to ZnO-Ts we added a certain amount of Mg powder to Zn. The evaporation temperature was set to 700 °C, because at these conditions best ZnO-T morphology was obtained. The partial vapor pressures of the gas phase species were calculated from the equilibrium vapor pressures, P^o, of pure metals (Mg and Zn) at the evaporation temperature and their mole fractions, x_i, in the powder mixture according to the Raoult's law:

$$P_i = P_i^o \cdot x_i. \quad (1)$$

The Mg vapor mole fraction y_{Mg} was determined as:

$$y_{Mg} = \frac{P_{Mg}}{P_{Mg}+P_{Zn}} \cdot 100\%. \quad (2)$$

TEM observation of the produced structures revealed that the introduction of Mg vapor results in the change of tetrapod dimensions. Statistical measurements (each sample of around 100 counts) on the basis of TEM images revealed that the tetrapods synthesized at y_{Mg} = 0% had the average leg diameter of 11.0 ± 5.0 nm and the length of 296 ± 192 nm, whereas the structures prepared at y_{Mg} = 2.3% were slightly larger with the respective dimensions of 16.5 ± 4.8 nm and 603 ± 221 nm. This effect can be explained by lowering Zn partial pressure in the reaction zone, which increases the nucleation critical size, which in turn determines the larger ZnO-T leg diameter.

X-Ray Diffraction (XRD) measurements showed that ZnO-Ts have wurtzite structure with the lattice constants of $a = b$ = 0.324 nm and c = 0.519 nm (Fig. 5). It is worth noting that Mg vapor did not result in any phase changes except for the sample synthesized at the highest Mg vapor concentration of y_{Mg} = 4.5%, where the appearance of the strongest MgO (200) peak in the XRD spectrum shows MgO segregation into separate crystalline phase. This shows, that $Zn_XMg_{(1-X)}O$ solid solution is formed, but when Mg vapor pressure reaches critical value, MgO phase is segregated. It can be also noted that absorbance and PL spectrum of the sample, produced at y_{Mg} = 4.5% has different shape, compared to samples produced at smaller amount of Mg.

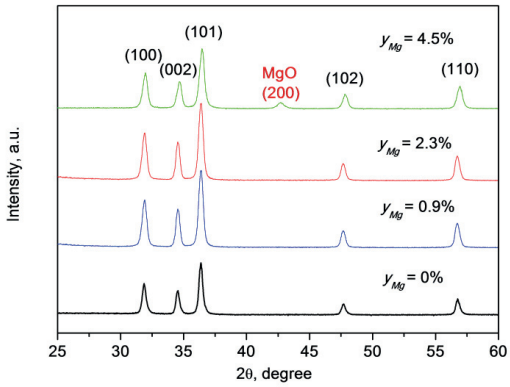

Figure 5. XRD spectra of ZnO tetrapods synthesized at different Mg vapor mole fraction, y_{Mg}.

From optical absorbance measurements (Fig. 6) it can be seen that the peak around 375 nm is shifted towards higher energies with increasing the Mg vapor concentration. Similar rather small (about 5 nm) blue shift was found in photoluminescence (PL) spectra (Fig. 7) for near band edge (NBE) emission peak. It is known, that adding Mg to ZnO significantly increases bandgap [28]. In our case during synthesis Mg is oxidized and solid solution $Zn_XMg_{(1-X)}O$ is formed. At higher Mg vapor pressure, amount of MgO in ZnO increases, until it reaches solubility limits and forms separate phase. The bandgap of $Zn_XMg_{(1-X)}O$ solid solution increases as MgO has larger bandgap, but in the PL spectra we do not observe monotonic blueshift of NBE peak, as higher Mg amount at the same time increases the diameter of the ZnO-T legs. For this reason NBE peak is affected by two processes at the same time: blueshift because of bandgap change and decreasing of the bandgap due to quantum confinement effect decrease.

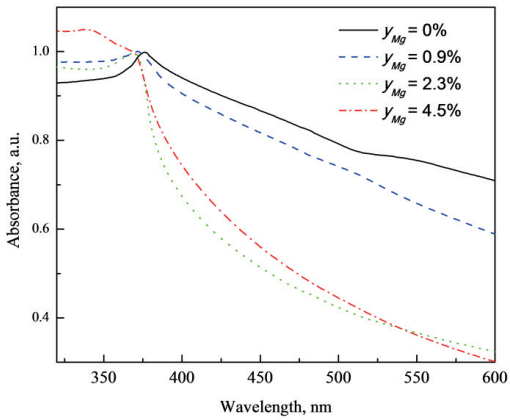

Figure 6. Absorbance spectra of ZnO tetrapods synthesized at different Mg vapor mole fraction, y_{Mg}.

It can be noted from the spectra presented in Fig. 6 that the absorbance in the visible range is decreased for higher y_{Mg}. This was also observed as the decrease of the peak at 425 nm with increasing the Mg vapor mole fraction (Fig. 7). Emission peak centered at around 425 nm(or 2.90 eV) is regarded as native shallow donor and associated to the transition between Zn interstitial level and valence band [29]. Zn interstitials are predominant defects because of the Zn vapor rich conditions in synthesis zone. Increase of Mg vapor mole fraction decreases Zn partial pressure and amount of Zn interstitials, which leads to decrease in shallow donor emission. Sonication of ZnO-T in ethanol may lead to hydrogen passivation of radiative recombination centers induced by O-Zn defects on the surfaces, as it has been previously shown for sonication in methanol [30].

In order to estimate the best synthesis conditions for transparent UV sensor application we calculated the quality factor, Q, which is defined as a ratio of transmittances at the wavelengths of 550 (T_{550}) and 375 nm (T_{375}), i.e.

$$Q = \frac{T_{550}}{T_{375}}. \quad (3)$$

ZnO-Ts synthesized at y_{Mg} = 2.3% had the highest quality factor of 4.30, compared to 1.76 and 2.20 for tetrapods respectively synthesized at y_{Mg} = 0 and y_{Mg} = 0.9%. It is worth noting that the sample synthesized at y_{Mg} = 4.5% with the quality factor of Q = 4.35 was not used for the UV sensor application due to the MgO phase segregation.

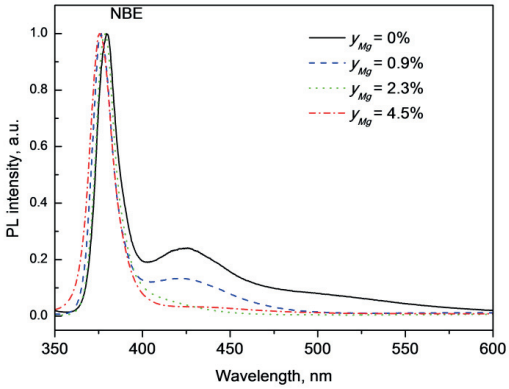

Figure 7. PL spectra of ZnO tetrapods synthesized at different Mg vapor mole fraction, y_{Mg}.

3.3. UV sensing

UV sensing phenomenon originates from the alteration of the charge carrier density. Under the UV-light irradiation with higher energy than the band gap of ZnO, the charge carrier density is increased, which reduces the resistance of ZnO tetrapods. When UV illumination is switched off, the oxygen chemisorption process dominates and assists photoconductivity relaxation [11].

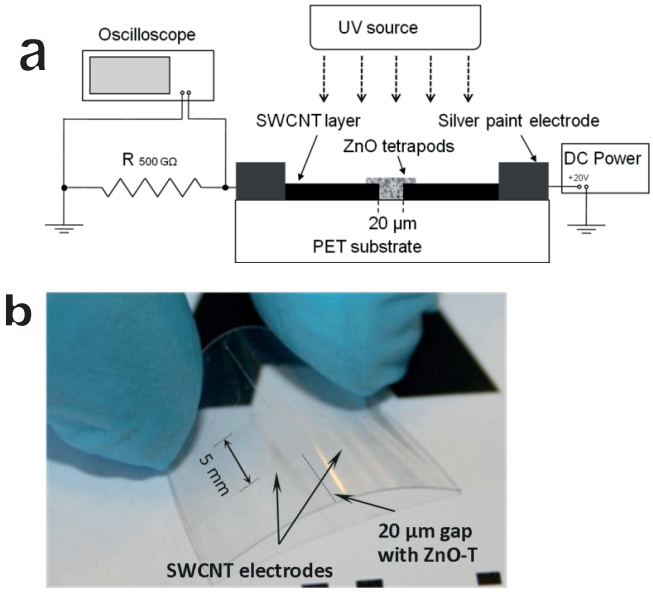

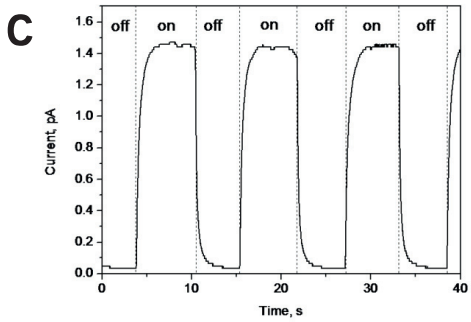

Figure 8. ZnO-T UV sensor: a) schematics of UV response measurement; b) a photo of the sensor; c) the sensor response to excitation at 365 nm.

UV sensor response was measured with a digital oscilloscope (Tektronix DPO 2014) by a comparison method, where the magnitudes of the reference resistor and the UV sensor were compared by the voltage drop they inflicted to the circuit (Fig. 8a). A constant potential (20 V) was applied over UV sensor and the reference resistor (500 GΩ) connected in series. The voltage drop over the reference resistor was recorded in time while UV illumination was turned on and off. Current flowing through the circuit was later resolved by applying Kirchhoff's law.

A flexible transparent UV sensor (Fig. 8a) was made by drying droplet of ZnO-T solution in ethanol between two transparent single-wall carbon nanotube (SWCNT) film contacts, on a polyethylene terephthalate (PET) substrate. SWCNT electrode fabrication is described elsewhere [31, 32], shortly, a one step process was used, filtered SWCNTs without any post processing were transferred from a filter by pressing it onto PET substrate. To obtain high optical transparency, sample synthesized at y_{Mg} = 2.3% and SWCNT electrodes with 95% transparency were used. UV sensing experiments were made under UV intensity of 30 μW/cm^2 at the wavelength of 365 nm. Fig. 8c shows a UV sensor response to the illumination. Initial current 0.032 pA increased to 1.45 pA under the UV illumination, which is 45 fold change. Response time to 90% of current change was 0.9 s.

Our UV sensor configuration leads to potential barriers, formed at the interfaces and junctions in the device (Fig 9): i) SWCNT electrode and ZnO-T junction, ii) multiple ZnO-T leg to leg junctions, iii) interface between ZnO wurtzite legs and zinc blende core. Work function of SWCNT electrode is 4.8 eV [33], and the electron affinity of ZnO is 4.5 eV [34], so Schottky barrier between ZnO-Ts and SWCNTs is formed. Depletion layers at the ZnO-T leg surface induced by electron trapping form another multiple leg to leg potential barriers. The interface between wurtzite legs and zinc blende core may also play a role in the transport mechanism as the contact barrier at the interface might lead to higher resistance, on the other hand the volume of the zinc blende core can be negligibly small and make no considerable influence.

High performance of the device, comparing to a single ZnO-T ohmic contact sensors [11, 35] is associated with the multiple barriers. The local electric field at the barrier area reduces the electron-hole recombination rates, resulting in an increase in free carrier density. Moreover, the UV-illumination-induced desorption of oxygen at the boundary changes the barrier height and narrows the barrier width, and also improves UV sensitivity. Rapid photocurrent response and recovery is related to quick changes interfacial region, instead of the whole surface [36, 37]. It is also known, that the higher the potential barrier, the faster the current recovery [38].

Response measurements show that such a photosensor is suitable for detection of low levels of UV light. Moreover the high resistance of 60 TΩ in the off state shows great potential for practical application in UV sensing.

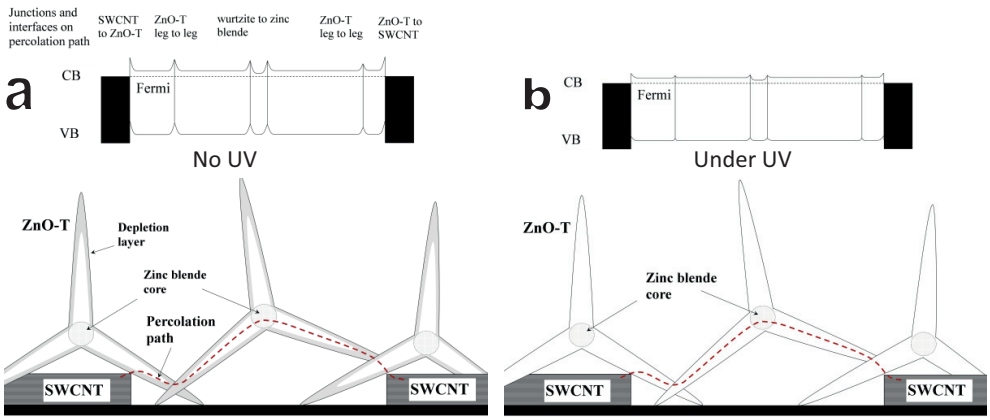

Figure 9. Schematics of barriers on ZnO-T UV sensor percolation path: a) no UV illumination; b) under UV. CB and VB mean conduction and valance band respectively.

4. Conclusions

In summary, we have designed and constructed a vertical flow reactor for controlled synthesis of ZnO-T structures. It was shown that morphology of ZnO-Ts can be adjusted by Zn vapor pressure in the reactor by changing the evaporation temperatue. The highest aspect ratio of single crystal ZnO-T structure is obtained at 700 °C. Mg introduction increases the band gap of ZnO-Ts and also increases visible range transparency. At y_{Mg} = 4.5% MgO segregates in a separate crystalline phase. ZnO-Ts with Mg have 16.5 nm diameter and 603.3 nm length legs, respectively compared to 11.0 nm and 296 nm for the Mg free ZnO-Ts. ZnO-Ts with Mg demonstrate application possibilities for transparent and flexible UV sensors show 45 fold current increase under UV irradiation with the intensity of 30 μW/cm^2 at the wavelength of 365 nm and response time of 0.9 s. High performance of the device is determined by multiple contact barriers.

Acknowledgements

This work was supported by the Academy of Finland (project No. 128445), EU FP7 project NANODEVICE (No. 211464) and Aalto University through the Multidisciplinary Institute of Digitalization and Energy (CNB-E project) programme.

References

1. Newton, M.C. and P.A. Warburton, *ZnO tetrapod nanocrystals.* Materials Today, 2007. **10**(5): p. 50-54.
2. Wang, Z.L. and J.H. Song, *Piezoelectric nanogenerators based on zinc oxide nanowire arrays.* Science, 2006. **312**(5771): p. 242-246.
3. Rackauskas, S., et al., *Mechanistic investigation of ZnO nanowire growth.* Applied Physics Letters, 2009. **95**(18): p. -.
4. Pan, Z.W., Z.R. Dai, and Z.L. Wang, *Nanobelts of semiconducting oxides.* Science, 2001. **291**(5510): p. 1947-1949.
5. Lao, J.Y., et al., *ZnO nanobridges and nanonails.* Nano Letters, 2003. **3**(2): p. 235-238.
6. Leung, Y.H., et al., *Zno nanoshells: Synthesis, structure, and optical properties.* Journal of Crystal Growth, 2005. **283**(1-2): p. 134-140.
7. Calestani, D., et al., *Growth of ZnO tetrapods for nanostructure-based gas sensors.* Sensors and Actuators B-Chemical, 2010. **144**(2): p. 472-478.
8. Ding, Y., et al., *Zinc-blende ZnO and its role in nucleating wurtzite tetrapods and twinned nanowires.* Applied Physics Letters, 2007. **90**(15): p. -.
9. Hsu, Y.F., et al., *Dye-sensitized solar cells using ZnO tetrapods.* Journal of Applied Physics, 2008. **103**(8): p. -.
10. Li, L.E. and L.N. Demianets, *Room-temperature excitonic lasing in ZnO tetrapod-like crystallites.* Optical Materials, 2008. **30**(7): p. 1074-1078.
11. Lupan, O., L. Chow, and G.Y. Chai, *A single ZnO tetrapod-based sensor.* Sensors and Actuators B-Chemical, 2009. **141**(2): p. 511-517.

12. Ronning, C., et al., *Nucleation mechanism of the seed of tetrapod ZnO nanostructures.* Journal of Applied Physics, 2005. **98**(3): p. -.
13. Shen, L., H. Zhang, and S.W. Guo, *Control on the morphologies of tetrapod ZnO nanocrystals.* Materials Chemistry and Physics, 2009. **114**(2-3): p. 580-583.
14. Wan, Q., et al., *Low-field electron emission from tetrapod-like ZnO nanostructures synthesized by rapid evaporation.* Applied Physics Letters, 2003. **83**(11): p. 2253-2255.
15. Wang, F.Z., et al., *Rapid synthesis and photoluminescence of novel ZnO nanotetrapods.* Journal of Crystal Growth, 2005. **274**(3-4): p. 447-452.
16. Wang, F.Z., et al., *Novel morphologies of ZnO nanotetrapods.* Materials Letters, 2005. **59**(5): p. 560-563.
17. Yamamoto, H., et al., *Generation of uniform tetrapod-shaped zincoxide nanoparticles by gas-phase reaction with using flow restrictor.* Advanced Powder Technology. **In Press, Corrected Proof**.
18. Yu, W.D., X.M. Li, and X.D. Gao, *Catalytic synthesis and structural characteristics of high-quality tetrapod-like ZnO nanocrystals by a modified vapor transport process.* Crystal Growth & Design, 2005. **5**(1): p. 151-155.
19. Zanotti, L., et al., *Vapour-phase growth, purification and large-area deposition of ZnO tetrapod nanostructures.* Crystal Research and Technology, 2010. **45**(6): p. 667-671.
20. Sirbuly, D.J., et al., *Semiconductor nanowires for subwavelength photonics integration.* Journal of Physical Chemistry B, 2005. **109**(32): p. 15190-15213.
21. Yin, Y. and A.P. Alivisatos, *Colloidal nanocrystal synthesis and the organic-inorganic interface.* Nature, 2005. **437**(7059): p. 664-670.
22. Yan, H.Q., et al., *Morphogenesis of one-dimensional ZnO nano- and microcrystals.* Advanced Materials, 2003. **15**(5): p. 402-+.
23. Zhang, Z., et al., *Controlling the growth mechanism of ZnO nanowires by selecting catalysts.* Journal of Physical Chemistry C, 2007. **111**(47): p. 17500-17505.
24. Morin, S.A., et al., *Mechanism and Kinetics of Spontaneous Nanotube Growth Driven by Screw Dislocations.* Science, 2010. **328**(5977): p. 476-480.
25. Watt, J., et al., *Synthesis and Structural Characterization of Branched Palladium Nanostructures.* Advanced Materials, 2009. **21**(22): p. 2288-+.
26. Penn, R.L., *Kinetics of oriented aggregation.* Journal of Physical Chemistry B, 2004. **108**(34): p. 12707-12712.
27. Cozzoli, P.D., et al., *ZnO nanocrystals by a non-hydrolytic route: Synthesis and characterization.* Journal of Physical Chemistry B, 2003. **107**(20): p. 4756-4762.
28. Wang, Y.S., P.J. Thomas, and P. O'Brien, *Optical Properties of ZnO Nanocrystals Doped with Cd, Mg, Mn, and Fe Ions.* The Journal of Physical Chemistry B, 2006. **110**(43): p. 21412-21415.
29. Janotti, A. and C.G. Van de Walle, *Native point defects in ZnO.* Physical Review B, 2007. **76**(16): p. 165202.
30. Marcus, C.N. and et al., *Synthesis and characterisation of zinc oxide tetrapod nanocrystals.* Journal of Physics: Conference Series, 2006. **26**(1): p. 251.
31. Nasibulin, A.G., et al., *Multifunctional Free-Standing Single-Walled Carbon Nanotube Films.* ACS Nano, 2011: p. null-null.
32. Kaskela, A., et al., *Aerosol-Synthesized SWCNT Networks with Tunable Conductivity and Transparency by a Dry Transfer Technique.* Nano Letters, 2010. **10**(11): p. 4349-4355.
33. Suzuki, S., et al., *Work functions and valence band states of pristine and Cs-intercalated single-walled carbon nanotube bundles*. Vol. 76. 2000: AIP. 4007-4009.
34. Song, J., J. Zhou, and Z.L. Wang, *Piezoelectric and Semiconducting Coupled Power Generating Process of a Single ZnO Belt/Wire. A Technology for Harvesting Electricity from the Environment.* Nano Letters, 2006. **6**(8): p. 1656-1662.
35. Lupan, O., et al., *Focused-ion-beam fabrication of ZnO nanorod-based UV photodetector using the in-situ lift-out technique.* Physica Status Solidi a-Applications and Materials Science, 2008. **205**(11): p. 2673-2678.
36. Hu, Y., et al., *Supersensitive, Fast-Response Nanowire Sensors by Using Schottky Contacts.* Advanced Materials, 2010. **22**(30): p. 3327-3332.
37. Zhou, J., et al., *Gigantic enhancement in response and reset time of ZnO UV nanosensor by utilizing Schottky contact and surface functionalization.* Applied Physics Letters, 2009. **94**(19): p. -.

38. Yanbo, L. and et al., *Bascule nanobridges self-assembled with ZnO nanowires as double Schottky barrier UV switches.* Nanotechnology, 2010. **21**(29): p. 295502.